(1)

II. SURFACE TREATMENT FOR INHIBITION OF CORROSION AND MITIGATION OF HYDROGEN ABSORPTION INTO INCONEL 718

B. N. Popov, G. Zheng and R. E. White

Department of Chemical Engineering

University of South Carolina

Columbia, SC 29208

1 FEB 92 - 31 JAN 93

Abstract

Polarization experiments show that monolayers of zinc, bismuth and lead inhibit effectively the hydrogen evolution reaction and hydrogen penetration through Inconel–718. The observed inhibition effects are due to the kinetic limitations of the hydrogen discharge reaction and suppression of hydrogen absorption on the deposited monolayers. The measured hydrogen penetration into a Inconel-718 membrane as determined by the Devanathan - Stachurski bipolar electrode technique, is suppressed due to the lower binding energy of hydrogen adatoms on lead, bismuth and zinc adsorbates. It is shown that the best inhibiton of the hydrogen permeation rate through an Inconel–718 membrane is obtained by a potentiostatically deposited bismuth monolayer which reduces the steady state hydrogen flux by 76%.

Introduction

High strength alloys are required to meet improved levels of corrosion resistance in naval applications. Their practical use is limited by cracking hazards due to hydrogen penetration and hydrogen accumulation in the bulk of these alloys (1–2). The irreversible accumulation of hydrogen in the bulk of the alloy leads to deterioration of its mechanical properties (2–7). Also in the presence of absorbed hydrogen, changes occur in both the lattice structure and the chemical composition of the alloy (8).

Pound (9) studied by using electrochemical methods the hydrogen ingress in high-strength alloys (AISI 4340 steel, Monel K500, and MP35N). The diffusion/trapping model for hydrogen ingress was shown to be applicable to the steel and Ni based

alloys. The rate of ingress in all three alloys was controlled by the flux across the interface. Pound (10) using a potentiostatic pulse technique, also studied the ingress of hydrogen in precipitation-hardened alloys (Inconel 718, Incoloy 925). Again his data were shown to fit a diffusion/trapping model under interface control.

Various methods have been proposed to decrease hydrogen embrittlement (2–4). However, it is impossible to reduce hydrogenation of the alloy substrate to a level which provides the elimination of hydrogen cracking hazards. However, it has been shown that underpotential deposited zinc, lead and bismuth on different substrates inhibit the discharge of hydrogen ions at an iron substrate (11–18). It has been shown this process is very important for corrosion behavior of metals (19), for electrocatalytic surface effects (20), for nucleation and crystal growth (21–22), and for plating (23).

The objective of this work was to estimate the effectiveness of underpotential deposition of Zn, Pb, and Bi onto Inconel 718 on the reduction in the corrosion rate and the degree of hydrogenation ingress. It was expected that these monolayers would reduce the surface coverage of adsorbed hydrogen due to the lower binding energy of the hydrogen adatoms on Zn, Bi and Pb adsorbates thereby reducing the absorption of hydrogen into Inconel 718.

Experimental

The electrochemical cell employed for these studies was a conventional three-compartment design with contact between the working electrode compartment and the reference electrode via a Luggin probe. The polarization experiments were carried out

using Inconel-718 steel rotating disc electrode with a geometric area of 0.5 cm^2. The electrode was mechanically polished to a fine finish, activated in sulfuric acid, washed with ethanol and in doubly distilled water.

Using the Devanathan-Stachurski permeation technique (24), both the rate of hydrogen absorption and permeation through Inconel-718 was measured continuously as a function of time. The permeation rate through a thin membrane of the alloy was measured by setting the potential on the "diffusion side" of the membrane (the side from which the hydrogen emerges) at a value which corresponds to a practically zero concentration of absorbed atomic hydrogen on the surface. This condition is maintained by instantaneous ionization of all hydrogen atoms which have diffused through the membrane and have emerged on the diffusion side. The measured current is directly proportional to the hydrogen permeation rate, which can be measured conveniently with a high degree of accuracy and sensitivity. These experiments were carried out in a system with two working compartments, separated by a bipolar Inconel–718 membrane. The Inconel-718 membrane with thickness of 50μm was obtained from Goodfellow Corp. The alloy membrane on the cathodic side of the cell was polarized potentiostatically, creating conditions for underpotential deposition and hydrogen evolution. The following reference electrodes were used: in the anodic compartment Hg/HgO; in the cathodic compartment $Hg/HgSO_4$ or SCE. In the anodic compartment of the cell, the membrane was polarized potentiostatically at –0.3 V vs Hg/HgO reference electrode and the amount of oxidized atomic hydrogen was monitored continuously using a chart recorder. The details of the permeation cell

and the auxiliary equipment are described by Subramayan (1). Prior to the permeation experiments, the Inconel-718 membrane with a thickness of 0.3 mm was mechanically polished to a fine finish, saturated with hydrogen in 0.1 M H_2SO_4 by maintaining for 10 hours a cathodic current density of 10 mA/cm^2. Then, the membrane was etched for 20 seconds in a solution containing methyl alcohol and 1% H_2SO_4, rinsed with distilled water, dried in air and fitted into the permeation cell. To avoid passivation or dissolution, the anodic side of the membrane was coated with a thin layer (0.15–0.20 μm) of palladium by electrodeposition. The deposition was carried out in an electrolyte containing $2x10^{-5}$ M $Na_2Pd(NO_2)_4$ using a current density of 100$\mu A/cm^2$ for two hours. Then, the electrolyte was drained off, the compartment washed with distilled water and filled with the anodic solution (0.2M NaOH), which was preelectrolyzed for at least 24 hours in a separate electrolytic cell. In the anodic compartment the solution was kept at –0.3 V vs Hg/HgO reference electrode until the background current was reduced to less than 3$\mu A/cm^2$. Then, the cathodic compartment was filled with the supporting electrolyte and the experiment was carried out. Pre-purified nitrogen was bubbled through both compartments in order to keep free of dissolved oxygen.

Results and Discussion

Cyclic Voltammetry. According to the coupled discharge-recombination mechanism for the rate of hydrogen evolution reaction (25), a possibility exists for the determination of the difference between hydrogen atoms that diffuse in the bulk of the alloy and those which participate in the molecular hydrogen evolution. During the electrocrystallization of metals onto foreign substrates, an underpotential deposition

with a formation of monoatomic layers with a definite structure often occurs prior the formation of a bulk deposit (26). It can occur when ions of a lower work-function metal are in the contact with a higher work function metal (27). The underpotential deposition has been reported and described to be restricted to monolayer or submonolayer deposition. It may be presumed that a partial submonolayer of underpotentially deposited zinc, bismuth or lead on the surface of the alloy will inhibit the hydrogen reaction due to the kinetic limitations of the hydrogen discharge reaction on the deposited monolayers.

An attempt was made by using cyclic voltammetry to test the validity of this presumption. Zinc was deposited from electrolyte containing: 1M Na_2SO_4, 0.4 M NaCl and 1 M H_3BO_3, pH=4. The concentration of zinc the electrolyte was gradually increased from $5x10^{-4}$ to 0.1 M and the voltammograms which were obtained at sweep rates of v= 1mV/s and 500 mV/s are shown in Figure (1) and Figure (2), respectively. In both Figures, a decrease of the hydrogen evolution is observed when the polarization was carried out in the presence and absence of zinc ions in the electrolyte. When starting the cathodic sweep from –0.2 V vs SCE a cathodic peak at –1.150 V is observed as shown in Figure (1) for a 0.1M Zn(II)n solution. The peak potential is more negative than the Nernst potential of a zinc electrode and corresponds to the diffusion controlled limiting wave of zinc reduction. The corresponding stripping peak appears at –0.9 V (SCE). In Figure (2), the zinc deposition peak from for a 0.1M Zn(II) disappears due to the increased peak separation which is obtained at the higher sweep rate. However, in the anodic part of the curve a well defined zinc

stripping and zinc desorption peak are observed in the range between -1.0V (SCE) and –0.7V (SCE) indicating that zinc probably is underpotential deposited on Inconel–718. Since the Nernst potential of zinc electrode is by E= –1.004 + 0.029 lg [Zn^{+2}], where [Zn^{+2}] is the concentration of Zn(II) in M/L, the zinc deposition from the bulk of the electrolyte should shift in cathodic direction for lower concentrations of zinc ions in the electrolyte. This phenomena is observed in Figure (2), where the corresponding stripping peaks for $5x10^{-3}$M Zn^{+2}; $5x10^{-2}$M Zn^{+2} and 0.1 M Zn^{+2} are observed at –1.040 V (SCE), –0.800 V (SCE) and at –0.750 V (SCE), respectively. The amount of charge was determined from the area of the desorption peaks for $5x10^{-3}$M Zn^{+2}; and $5x10^{-2}$M Zn^{+2} and are: 115 $\mu C/cm^2$ and 95 $\mu C/cm^2$ respectively. Presuming that the maximum coverage requires a charge of $Q_{max} = 450\mu A/cm^2$ (18), the degree of coverage by zinc ($\theta_{Zn,\,ads}$) for the desorptions peaks are 0.25 and 0.21 for Zn^{+2} concentrations, of the first and second respectively.

Bismuth deposition on Inconel 718 rotating disc electrode was studied from electrolyte containing: 0.5 M $HClO_4$, 0.25 M $NaCl_4$ at pH=0.3 and the metal ion concentration in the range of $2x10^{-5}$ to $5x10^{-4}$M. The maximum concentration of bismuth ions in the electrolyte depends on the solubility product of Bi_2O_3. The cathodic sweep in Figure (3) starts at 0.2 V vs SCE, the vertex potential is at –0.5 V, and the scan ends at 0.4 V (SCE). In the presence of bismuth ions in the electrolyte, a well defined cathodic peak is observed at –0.150 V vs SCE. Since the steady–state limiting current corresponding to the deposition of bulk bismuth metals from $2x10^{-5}$M solution of Bi^{+3} has a half-wave potential of –0.1 V (SCE), the observed process at

–0.150 V vs SCE corresponds to the deposition of bulk bismuth metal. The integrated area under the cathodic peaks increase with the increase of bismuth ion concentration and are : 75 $\mu C/cm^2$, 130 $\mu C/cm^2$, and 230 $\mu C/cm^2$ computed for $5x10^{-5}M$, $2x10^{-4}M$ and $5x10^{-4}M$ Bi^{+3}, respectively. According to Cadle et al. (17), a plot of the bismuth convective diffusion current measured on platinum in 0.12 M perchloric solutions at –0.2 V vs SCE vs. $\omega^{1/2}$, (the square root of the angular velocity of the electrode) is linear. Using the Newman version of the Levich equation, the slope of the Levich plot at this potential gives a value of 5.5 $x10^{-6}$ cm^2/s for the diffusion coefficient of bismuth ions. The small positive non-zero intercept observed was attributed to the hydrogen discharge current. In the anodic branch of the curve, two stripping peaks are observed. The first anodic peak corresponds to the oxidation of bismuth, previously deposited by the convective-diffusion controlled limiting wave for bismuth reduction. As it was expected, according to the Nernst behavior of bismuth electrode, the bismuth stripping peak in Figure (3) shifts in the positive direction with the increase of bismuth ion concentration in the electrolyte. The amount of the charge under the peaks also increases with the increase of the concentration of Bi^{+3}species in the solution and are: 200 $\mu A/cm^2$; 1000 $\mu A/cm^2$; and 2000 $\mu A/cm^2$ for $5x10^{-5}M$, $2x10^{-4}M$ and $5x10^{-4}M$ Bi^{+3}, respectively. The initial Bi^{+3} reduction occurs probably simultaneously with the reduction of the oxide present on Inconel–718 surface and presumably Bi(0) is deposited on a reduced surface as in the case of reported deposition of Bi^{+3} on platinum electrode (17). If the Inconel–718 rotating disc electrode is potentiostated at any potential between +0.25 V and –0.1 V (SCE) in a $5x10^{-5}$ Bi^{+3} solution, the

reduction current from 85 $\mu A/cm^2$ falls to zero within 90 seconds. Probably, the current between +0.25 V and –0.1 V (SCE) and the small maximum in Figure (3), observed prior the bismuth deposition peak from the bulk, reflects the simultaneous adsorption of bismuth and hydrogen and corresponds to the underpotential deposited Bi(0). Consequently, the second anodic peak which appears at + 0.2 V vs SCE should correspond to the stripping peak of the underpotentially deposited Bi. Similar results were obtained by Cadle et al. (17), who studied the reduction of bismuth on platinum using ring disc electrode. According to their study, current–potential curves of Bi^{+3} in 0.12M perchloric acid show three reduction processes in the cathodic potential scan and several oxidation processes in the anodic scan. The cathodic processes were found to represent the reduction of adsorbed bismuth, reduction of bismuth at underpotential and the convective - diffusion controlled limiting wave for bismuth reduction. The anodic processes were explained as the oxidation of the bulk bismuth, the oxidation of surface layers of bismuth and oxidation of underpotential bismuth.

Figure (4) shows potentiodynamic curves obtained at different reverse potentials starting from 0.0 V (SCE). The vertex potentials of –0.350 and –0.400 V (SCE) were chosen in order to avoid the hydrogen evolution reaction. The area under the second anodic peak is 700 $\mu A/cm^2$ and corresponds approximately to a close packed monolayer of Bi(0) (17). Probably both the underpotential submonolayer of Bi(0) and the monolayer of Bi(0) are oxidized at the second anodic peak in Figure (4). They are deposited before any of the Bi(0) stripped at the first anodic peak in Figure (3) is plated on the electrode. The same phenomena was observed by Cadle et al. (17) for

the deposition of bismuth on platinum. On platinum it is also known (28) that two monolayers of copper or silver must be deposited before any behavior characteristics of the plating metal can be observed.

Cyclic voltammetry was also used to study the lead deposition on Inconel-718 alloy rotating disc electrode from perchlorate solutions. CV curves obtained in the absence and presence of lead in the supporting electrolyte are given in Figure (5). When starting the cathodic sweep at +0.050 V (SCE) only peaks on the anodic part of the polarization curve are observed. Since, the Nernst potential of lead electrode, $E = -0.368 + 0.029 \lg (5 \times 10^{-4}) = -0.45$ V vs SCE, the stripping peak at –0.4V vs SCE corresponds to dissolution of the bulk deposited lead. As seen in Figure (5), the peak height at –0.45 V (SCE) increases with the increase of lead concentration in the electrolyte indicating again that the peak is related to the bulk lead deposition. The second anodic peak probably can be attributed to the lead desorption peak of the underpotential deposited lead in the potential range between –0.2V (SCE) and –0.350V (SCE). The amount of charge of the deposited monolayer was computed from the area of the desorption peak and is $Q = 95\ \mu C/cm^2$. Assuming that the maximum coverage of Pb adatoms requires a charge of $Q_{max} = 500\ \mu C/cm^2$ (16,29), the degree of coverage by lead is $\theta = 0.19$. In Figure (6), the anodic peaks were analyzed for different reverse potentials. Data are not available for the work-function values of Inconel-718 in order to evaluate the theoretical conditions for the occurrence of underpotential deposition of lead. However, underpotential deposition of lead on platinum was verify by Cadle et al. (29) to occur at potentials ranging from –0.3 to +0.5 Vvs SCE. Cadle et al. (29)

also reported the inhibiting effect of underpotential deposited lead on the adsorption process of hydrogen at the metal substrate. Underpotential deposition of Pb^{+2} is invoked by Lafrancony et al. (16) as an explanation of the inhibition of the reaction step involving the adsorption step of hydrogen discharge on stainless steel alloy.

In Figure (6), the anodic peaks were analyzed for different reverse potentials. Since more lead is deposited at higher cathodic overpotentials, the lead stripping peak increases with the shift of the reverse potential in the cathodic direction.

Polarization Measurements-Potentiodynamic Studies. Cathodic polarization curves are shown in Fifgure (7) for hydrogen evolution reaction on bare Inconel-718 alloy from an electrolyte containing: 1M Na_2SO_4 + 0.4 M NaCl and 1M H_3BO_3 at pH=4 and on Inconel-718 alloy predeposited with Zn from the same supporting electrolyte in which $5x10^{-4}$M Zn^{+2} ions are added. In order to deposit zinc, the rotating disc electrodes (area=0.5 cm^2) were held at fixed cathodic current for a different periods of time to ensure that Zn was deposited on the surface. Various coverages were obtained by trial and error by applying a wide range of current densities. Thus, the range of current densities over which the additive deposition from the bulk of the electrolyte occurs was determined. Then currents, below the highest current at which underpotential occurs were used to obtain different surface coverages. The amount of charge required for monolayer deposition was determined by the area of the adsorption-desorption peaks observed in the potentiodynamic studies.

As shown in Figure (7), in the absence of zinc, a linear region with a Tafel slope of 125 mV which corresponds to α_c=0.42 was obtained indicating activation control

of h.e.r. in the potential region between –0.450 and –0.720 V vs SCE. The corrosion currents were obtained from the intersection of the cathodic Tafel line and the corrosion potential. A value of 11.4×10^{-6} A/cm^2 was obtained for the corrosion current of bare Inconle-718. Figure (7), also shows the shape of Tafel plots obtained for different for different degrees of surface coverages by zinc. The presence of zinc on the alloy surface inhibited the hydrogen evolution reaction with the increase of Tafel slope from 130 mV to 140 mV, α=0.41 and corrosion current of 8.5×10^{-6} A/cm^2. As seen in Figure (8), the curve obtained at –0.590 V (SCE), the hydrogen discharge currents on Inconel-718 alloy surface with deposited submonolayers of zinc is reduced by 70% compared with hydrogen discharge currents obtained for bare Inconel. In the case of Inconel-718, no zinc deposition could be thermodynamically probable under the experimental conditions. The standard potential for the reaction $Zn^{+2} + 2e = Zn$ is –1.004 V (SCE). Since E_{rev}=-1.004 +0.029 lg $a_{Zn^{+2}}$, when Zn^{+2} is 5×10^{-4} M, then $E_{rev\ Zn^{+2}/Zn}$ = –1.102V vs SCE which is more negative potential than the corrosion potential of the Inconel-718 [E_{corr}= –0.420 V (SCE)]. Thus, the possibility of zinc plating from the bulk of the solution was excluded. The absence of zinc plating on the alloy surface indicates that probably underpotential deposition of zinc influences the kinetics of the hydrogen evolution reaction.

The evolution of hydrogen was also studied potentiodynamically on Inconel-718 rotating disc electrode treated with Bi from electrolyte containing 5×10^{-4}M Bi_2O_3 + 0.5M $HClO_4$ and 0.25M $NaClO_4$. Figure (9) shows the Tafel slopes obtained for two different depositions currents and subsequently for different degree of surface

coverage by bismuth. In absence of bismuth in the supporting electrolyte a linear region of E vs log (i) was observed with a Tafel slope of 125 mV. The presence of Bi in the electrolyte decreases the hydrogen evolution rate with Tafel slope of 135 mV. A value of $9x10^{-6}A/cm^2$ was obtained for the corrosion current for bare Inconel –718. In the presence Bi adatoms a decrease of the corrosion current was observed with a value of $1.6\ x10^{-6}A/cm^2$.

The dependence of the hydrogen evolution current upon the predeposition current at which the bismuth monolayer was deposited is given in Figure (10). According to the data presented in this Figure, the bismuth adatoms on the alloy surface reduce the hydrogen discharge current by 65%.

Figure (11) shows polarization curves obtained on bare Inconel-718 rotating disc electrodes in the electrolyte containing : 0.5M $HClO_4$ and 0.25M $NaClO_4$ and polarization curves obtained on rotating Inconel-718 disc electrodes on which monolayer of lead was predeposited from lead containing electrolytes ($2x10^{-3}m\ Pb^{+2}$ using three different depositions currents. The presence of lead adatoms on the alloy surface at the potential range between –0.2 V (SCE) and – 0.010V (SCE), inhibited the h.e.r. The linear part of the polarization curve has a slope of 135 mV and α_c=0.47. The corrosion currents in the absence and presence of lead adatoms on the alloy surface are: $9x10^{-6}A/cm^2$ and $5x10^{-6}A/cm^2$, respectively.

The standard potential E^o for the reaction $Pb^{2+} + 2e \rightarrow Pb$, is –0.368 (SCE). Since $E_{rev\ Pb^{+2}/Pb} = -0.368 + 0.0295 \log a_{Pb^{+2}}$, when $[Pb^{+2}]$ is $2x10^{-3}M$, then $E_{rev,Pb^{+2}/Pb}$ is –0.448V (SCE), which is less noble than the corrosion potential of Inconel-718.

Accordingly, the lead deposition from the bulk of the electrolyte under the conditions at which the experiments were carried out was excluded.

As shown in Figure (12), the hydrogen evolution current, computed at –0.150V, (SCE) and at –0.080V (SCE) as a function of the predeposition current, is reduced by 63% and 61%, respectively. Tafel curves obtained on Inconel-718 with bulk deposited lead using different deposition currents for a period of seven minutes are presented in Figure (13). In the presence of bulk deposited lead the polarization behavior drastically changes. The corrosion potential from a value of –0.050V (SCE) in the presence of adatoms [Figure (12)] shifts in cathodic direction to a value of –0.425V, (SCE) when the lead is deposited conventionally. The bulk deposited lead also increases the corrosion current to a value of 115μA/cm^2, with a Tafel slope of 115mV and α=0.51.

The hydrogen evolution reaction has been widely studied and mainly two basic mechanism have been accepted (30). The recombination mechanism expressed as:

$$H^+ + e^- + M \rightarrowtail MH_{ads} \qquad (1)$$

$$MH_{ads} + MH_{ads} \rightarrowtail 2M + H_2 \qquad (2)$$

and the electrochemical desorption mechanism:

$$M + H^+ + e^- \rightarrowtail MH_{ads} \qquad (3)$$

$$MH_{ads} + H^+ + e \rightarrowtail H_2 + M \qquad (4)$$

According to Bockris et al. (25) and McBreen et al. (31), the hydrogen evolution reaction in acidic electrolytes is determined by the coupled discharge-recombination mechanism. Assuming the Langmuir adsorption isotherm, theoretically the discharge-recombination mechanism is released at low degree of surface coverage by atomic hydrogen (θ<0.1). The current-potential relationships obtained in this study in the presence of submonolayers of zinc, bismuth and lead on Inconel-718 showed slopes in the range of b=120 mV to 130 mV which corresponds to $\frac{2RT}{F}$ diagnostic criteria indicating that the hydrogen evolution reaction occurs via a coupled discharge-recombination. mechanism. This mechanism involves H_{ads} species and enhances the role of the hydrogen adsorption on the overall h.e.r. According to our study the observed reduction of the corrosion rate and the inhibition of the hydrogen discharge current results from the presence of underpotential deposited Zn, Bi or Pb. The underpotential deposited Zn, Bi and Pb inhibit the h.e.r. by increasing the hydrogen overvoltage and suppressing the hydrogen absorption due to the lower binding energy of the hydrogen adatoms on Pb, Bi and Zn adsorbates (11–19).

Hydrogen Permeation Studies. When carrying out experiments with a bipolar membrane, the steady sate rate of hydrogen penetration in a diffusion mode can be presented by the following equations obtained for two typical boundary conditions: (1) in the case when the hydrogen concentration at the entry side of the membrane is constant (30);

$$\frac{j_t - j_o}{j_\infty - j_o} = 1 + 2\sum_{n=1}^{\infty}(-1)^n exp(-n^2\pi^2\tau) \qquad (5)$$

(2) in the case when the flux of the hydrogen entering the membrane is constant (30);

$$\frac{j_t - j_o}{j_\infty - j_o} = 1 - \frac{4}{\pi}\sum_{n=0}^{\infty}\frac{(-1)^n}{(2n+1)}exp\left\{-\frac{(2n+1)^2\pi^2\tau}{4}\right\} \qquad (6)$$

where j_t = transition hydrogen permeation current density; j_o= initial hydrogen permeation current density (may or may not be zero); j_∞= steady state hydrogen permeation current density.

In the preliminary experiments, the hydrogen permeation transients were obtained in supporting electrolyte containing: 1M Na_2SO_4+0.4M NaCl +1M H_3BO_3 in the presence and absence of $5x10^{-4}$M Zn^{+2}. The permeation transients as a function of time are presented in Figure (14). The diffusion of hydrogen through the Inconel-718 membrane was calculated [by using the data at E_c=-0.690 V (SCE)] to be $3.2x10^{-11}$ cm^2/s. Similar results for the diffusivity were obtained by Robertson et al (32) for Fe-Ni alloys. In Figure (15), the hydrogen permeation current density vs the dimensionless time τ and the theoretical solutions for the two typical boundary conditions given above are presented for comparison with the experimental results shown in Figure 14). The results obtained for Inconel-718 membrane indicate that the hydrogen permeation transients are approaching the theoretical curve obtained by using boundary conditions in which the hydrogen concentration at the entry side of the membrane is constant. These results agree with those obtained by Archer et al. (33) who studied the hydrogen permeation through a nickel membrane.

As shown in our polarization studies, monolayer coverage of Zn, Bi and Pb adatoms on Inconel-718 rotating disc electrode cause a suppression of hydrogen

adsorption by changing chemically the surface without altering the mechanical or physical properties of the substrate. In order to investigate if any inhibition of the hydrogen permeation current occurs in the presence of the additives, the hydrogen permeation experiments were carried out in the presence of Zn^{+2}, Bi^{+3} and Pb^{+2} using in the cathodic compartment the same supporting electrolytes as those used in the polarization studies. Since our potentiodynamic studies indicated that the Zn underpotential deposition occurs at –1.0 V (SCE), the permeation experiments in the presence of 0.1 M Zn^{+2} ions were carried out at the same potential. The resulting hydrogen permeation transients are plotted in Figure (14). According to data presented in this Figure, the steady state hydrogen flux is reduced from 0.82 $\mu A/cm^2$ to 0.51 $\mu A/cm^2$ (a decrease of about 38%). This is partially due to the observed decrease of the steady state discharge current density (decreases from 0.48 mA/cm^2 to 0.21 mA/cm^2).

The hydrogen permeation through Inconel-718 membrane was also studied in the presence of Bi^{+3} and Pb^{+2} in the supporting electrolyte containing 0.5 M $HClO_4$ and 0.25M $NaClO_4$. In order to avoid the bulk deposition of Bi and Pb on the Inconel-718 substrate, the deposition was carried out at potentials which are more anodic than the reversible potentials of bismuth and lead. The resulting hydrogen permeation transients obtained in the presence and absence of bismuth ($5x10^{-4}$M Bi^{+3}) and lead ($2x10^{-3}$) are shown in Figure (16). In Figure (17), the hydrogen permeation current computed from the theoretical solutions of the typical boundary conditions for hydrogen permeation are presented for comparison with the results obtained experimentally as a function of the dimensionless time τ. In the presence of bismuth and lead ions in the supporting

electrolyte, the steady state hydrogen flux is reduced by 76% and 68%, respectively.

Iyer et al. (34–35) developed a mechanistic model [I-P-Z model] which considers the effect of hydrogen entry into a metal on the kinetics of the hydrogen evolution reaction (h.e.r). Using this model to describe the permeation transients in the presence and absence of additives in supporting electrolyte, one obtains:

$$j_{\infty,1} = \frac{k_1''}{b\sqrt{F k_{3,1}}}\sqrt{i_{r,1}} \tag{7}$$

$$j_{\infty,2} = \frac{k''}{b\sqrt{F k_{3,2}}}\sqrt{i_{r,2}} \tag{8}$$

where $j\infty$ = steady state hydrogen permeation current density, 1 and 2 denotes absence and the presence of the additives; k'' is thickness dependent absorption-adsorption constant, b=L/FD, L= the membrane thickness, D= hydrogen diffusion coefficient; k_3 is a recombination rate constant and i_r is hydrogen recombination current. Dividing the equations, one obtains:

$$\frac{j_{\infty,2}}{j_{\infty,1}} = \sqrt{\frac{i_{r,2}}{i_{r,1}}}\sqrt{\frac{k_{3,1}}{k_{3,2}}}\frac{k_{3,1}}{k_{3,2}} \tag{9}$$

According to Equation (9), the hydrogen permeation flux may be reduced due to: (1) the changes of the surface properties, i.e., the increase of the hydrogen recombination rate constant (k_3) or (2) by decreasing the absorption-adsorption constant k''. Our objective was to use additives to modify the surface in order to achieve favorable changes and to reduce the hydrogen permeation flux. Further work which will

clarify the contribution of the alloy surface properties such as the hydrogen recombination constant and the absorption-adsorption constant [when zinc, bismuth or lead are underpotentially deposited] on the hydrogen permeation is in progress.

Conclusion

Tafel and linear sweep voltammetry were used to study the hydrogen discharge on Inconel-718 with deposited submonolayers of zinc, bismuth and lead. The inhibition of hydrogen evolution reaction is explained by a suppression of hydrogen absorption due to the lower binding energy of the hydrogen adatoms on Zn, Pb and Bi adsorbates. As a consequence of the suppressed hydrogen absorption, the hydrogen penetration decreases in the bulk of the alloy.

Acknowledgment

Technical assistance and financial support by A. John Sedriks, the Office of Naval Research, under Contract No N00014-92-J-1434 are gratefully acknowledged.

Figure Captions

Figure (1) Potentiodynamic curves obtained on Inconel-718 rotating disc electrode for different concentrations of Zn^{+2}. Sweep rate, v=1 mV/s.

Figure (2) Potentiodynamic curves obtained on Inconel-718 rotating disc electrode for different concentrations of Zn^{+2}. Sweep rate, v=500mV/s.

Figure (3) Potentiodynamic curves obtained on Inconel-718 rotating disc electrode for different concentrations of Bi^{+3}. Sweep rate, v=100mV/s.

Figure (4) Potentiodynamic curves obtained on Inconel-718 rotating disc electrode at different vertex potentials. $C_{Bi^{+3}}= 5x10^{-4}M$. Sweep rate, v=100mV/s.

Figure (5) Potentiodynamic curves obtained on Inconel-718 rotating disc electrode for different Pb^{+2} concentrations. Sweep rate, v=100mV/s

Figure (6) Potentiodynamic curves obtained on Inconel-718 rotating disc electrode at different vertex potentials. Sweep rate, v=100mV/s, $C_{Pb^{+2}}= 2x10^{-3}M$.

Figure (7) Polarization curves obtained on bare Inconel-718 rotating disc

electrode from supporting electrolyte: 1M Na_2SO_4+0.4M NaCl + 1M H_3BO_3 at pH=4 and on zinc predeposited electrode from supporting electrolyte containing $5x10^{-}$M Zn^{+2}. Sweep rate, v=1mV/s.

Figure (8) Dependence of hydrogen evolution current computed at two different applied potentials upon the zinc predeposition current.

Figure (9) Polarization curves obtained on Inconel-718 rotating disc electrode on which bismuth was deposited using different predeposition currents from electrolyte containing: 0.5 M $HClO_4$ + 0.25M $NaClO_4$ + $5x10^{-4}$M Bi^{+3}. Sweep rate, v=1mV/s.

Figure (10) Dependence of hydrogen evolution current computed at –0.75V (SCE) upon the bismuth predeposition current.

Figure (11) Polarization curves obtained on bare Inconel-718 rotating disc electrode from electrolyte containing: 0.5M $HClO_4$ + 0.25M $NaClO_4$ and on electrodes with predeposited monolayers of lead from electrolyte containing $2x10^{-3}$M Pb^{+2}.Sweep rate, v=1mV/s.

Figure (12) Dependence of hydrogen evolution current computed at –0.150V

(SCE) and at -0.08V (SCE) as a function of the predeposition current. $C_{Pb^{+2}}$= $2x10^{-3}$M.

Figure (13) Tafel plots obtained on Inconel-718 rotating disc electrode with bulk deposited lead.

Figure (14) Hydrogen permeation transients as a function of time obtained in supporting electrolyte containing: 1M Na_2SO_4 + 0.4M NaCl + 1M H_3BO_3 in the presence and absence of $5x10^{-4}$M Zn^{+2}.

Figure (15) Computed and experimentally measured hydrogen permeation current as a function of the dimensionless time τ.

Figure (16) Hydrogen permeation transients as a function of time obtained in supporting electrolyte containing: 0.5M $HClO_4$+ 0.25M $NaClO_4$ in the presence and absence of lead and bismuth ions in the electrolyte.

Figure (17) Computed and experimentally measured hydrogen permeation transients as a function of the dimensionless time τ.

List of Symbols

$a = F/RT$, $(V)^{-1}$

$b = L/(FD_H)$, $(Acm)^{-1})$

D = hydrogen diffusion coefficient, $(cm^2\ s^{-1}$

F = Faraday constant, 96,500 C $(g\text{-}eq)^{-1}$

L = membrane thickness, (m)

i_o = exchange current density, (A cm^{-2}).

$i_o' = \frac{i_o}{1-\theta_c}$, (A cm^2)

j_t = transition hydrogen permeation current density, (A cm^{-2})

j_o = initial hydrogen permeation current density, (A cm^{-2})

j_∞ = steady state hydrogen permeation current density, (A cm^{-2})

k_{abs} = absorption rate constant, [mol $(cm^2 s)^{-1}$]

k_{ads} = adsorption rate constant, (cm s^{-1})

k_3 = recombination rate constant, [mol $(cm^2 s)^{-1}$]

k" = thickness dependent absorption-adsorption constant, (mol cm^{-3}).

Greek Symbols

α = transfer coefficient, dimensionless

θ_H = hydrogen surface coverage, dimensionless

η = overvoltage, (V).

$\tau = t\ D/L^2$ = dimensionless time

References

1. P. Subramanyan in ***Comprenhensive Treatise of Electrochemistry,*** J. O'M. Bockris, Brian E. Conway, Ernest Yeager and Ralph E. White, Eds., **4**, 411, Plenum Press, New York, (1981).
2. S. Bagaev and K. Pedan and V. Kudrjavtsev, ***Zatshtita Metallov*, 19**, 968 (1983).
3. V. Kudryatsev, K. Pedan, H. Barbashkina and S. Vagramjan, **ibid, 9**, 161, (1973).
4. W. Beck, J. Jankowski, P. Fisher, S. Williams and H. Bowen, ***Report NADC-MA-7140,*** New York, 560, (1971).
5. J. P. Hirth, ***Meall. Trans.*** **11A**, 861, (1980).
6. R. A. Oriani, ***Rev. Mater. Sci.*, 8**, 327, (1978).
7. J. J. Reilly, ***Z. Phys. Chem.*,117**, 655, (1979).
8. A. J. Kumnick and H. H. Johnson, ***Meall. Trans.*, 6A**, 1087, (1975).
9. B. G. Pound, ***Corrrosion, 45***, 18, (1989).
10. B. G. Pound, ***Acta Metall.*** **38**, 2373, (1990)
11. D. M. Drazic and L. Z. Vorkapic, ***Corrosion Science*, 18**, 907, (1978).
12. A. Despic and M. Pavlovic, ***Electrochim. Acta*, 27**, 1539, (1982).
13. K. Juttner, ***Werkst. Korros.*, 31**, 358, ((1980).
14. A. M. Abd El Halim, K. Juttner and W. J. Lorenz, ***J. Electroanal. Chem.*, 106**, 193, (1980).
15. N. Faruya and S. Motoo, ***ibid*, 70**, 165, (1976); **78**, 243 (1977); **88**, 151, (1978).
16. G. Lafranconi, F. Mazza, E. Sivieri and S. Torchio, ***Corrosion Scieence*, 18**, 617, (1978).

17. S. H. Cadle and S. Bruckenstein, ***Anal. Chem.***, **43**, 1858, (1971).

18. V. Kudryavtsev, K. Pedan and S. Bagaev, ***J. Electroanal. Chem.***, **248**, 421, (1988).

19. K. Juttner and W. Lorenc, ***J. Phys. Chem.*** **122**, 163, (1980).

20. R. Adzic, D. Simic, A. Despic and D. Drazic, ***J. Electroanal. Chem.*** **65**, 587, (1975).

21. A. Bewick, J. Jovicevic and B. Tomas, ***Faraday Symp. Chem. Soc.*****12**, 24, (1977).

22. N. Pangarov, ***Electrochim. Acta*****28**, 763, (1983).

23. M. Nicol and H. Philip, ***J. Electroanal. Chem.*****70**, 233, (1976).

24. M. A. V. Devanathan and L. Strachurski, ***Proc. R. Soc. London Ser***, **A 270**, 90, (1962).

25. J. O'M Bockris, J. McBreen and L. Nanis, ***J. Electrochem. Soc.***, **112**, 1027, (1965).

26. D. M. Kolb, M. Przasnyski and H. Gerisher, ***J. Electroanal. Chem.*****33**, 351, (1971).

27. S. Trasati, ***J. Physik. Chem.*** **75**, 1, (1975).

28. G. Kumar, J. R. Blackburn, R. G. Albridge, W. E. Moddeman and M. M. Jones, ***Inorg. Chem.*****11**, 296 (1972).

29. S. H. Cadle and S. Bruckenstein, ***Anal. Chem.*** **11**, 1858 (1971).

30. N. Boes and H. Zuchner, ***J. Less-Common Metals***, **49**, 223 (1976).

31. J. McBreen and A. M. Genshow, ***Proc. Conf. Fund Aspects of Stress Corrosion Cracking, NACE***, Columbus, OH, 51 (1969)

32. W. M. Robertson, ***Metall. Trans.*** **10A**, 489, (1979).

33. M. D. Archer and N. C. Grant, ***Proc. R. Soc. Lond.***, **A395**, 165 (1984).

34. R. N. Iyer, H. W. Pickering and M. Zamanzadeh, ***J. Electrochem. Soc.***, **136**, 2463, (1989).

35. R. N. Iyer, H. W. Pickering and M. Zamanzadeh, ***Scripta Metallurgica***, **22**, 911, (1988).

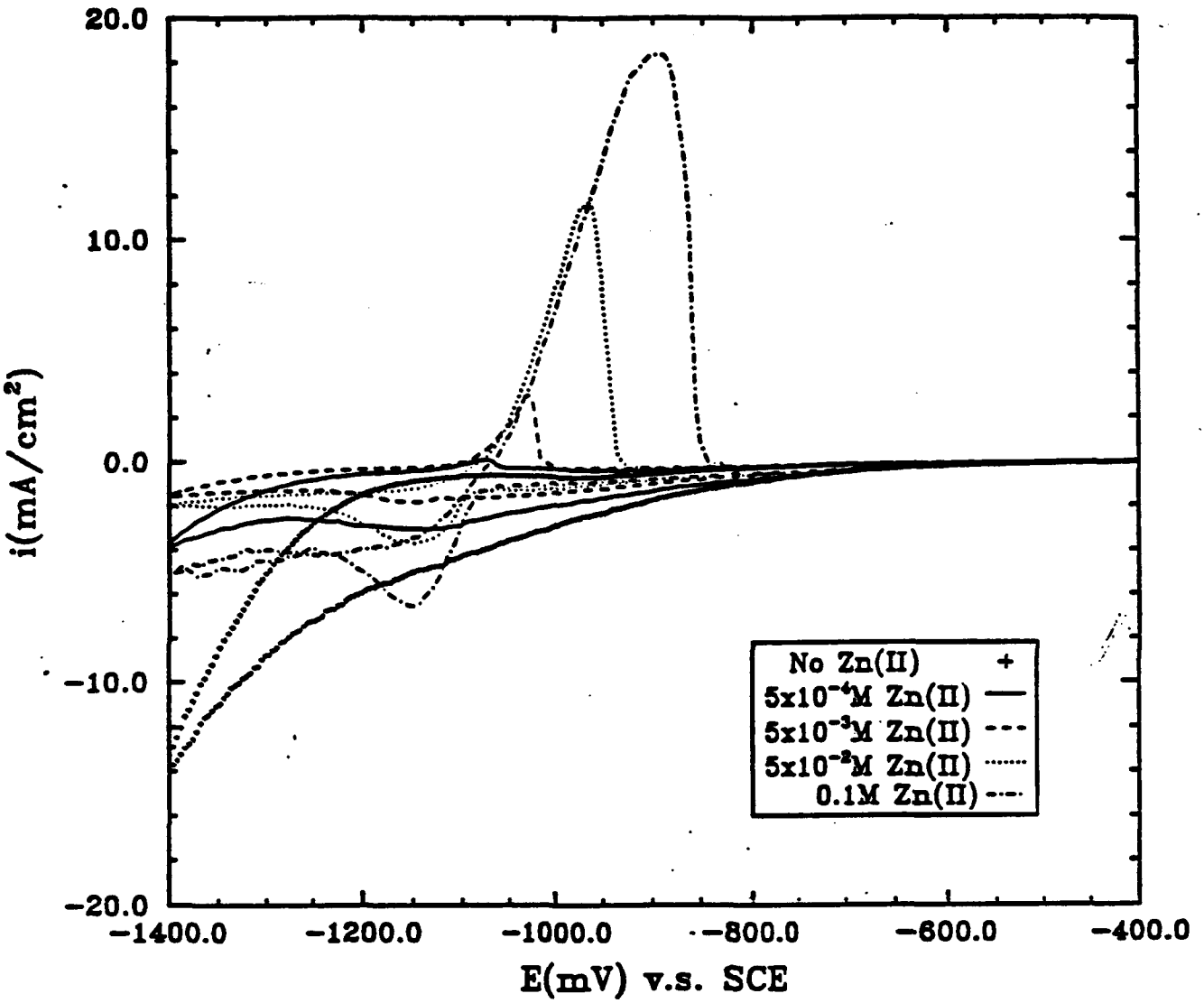
20.0
10.0
0.0
-10.0
-20.0
i(mA/cm²)
-1400.0
-1200.0
-1000.0
-800.0
-600.0
-400.0
E(mV) v.s. SCE
No Zn(II)
5x10⁻⁴M Zn(II)
5x10⁻³M Zn(II)
5x10⁻²M Zn(II)
0.1M Zn(II)

Figure 1

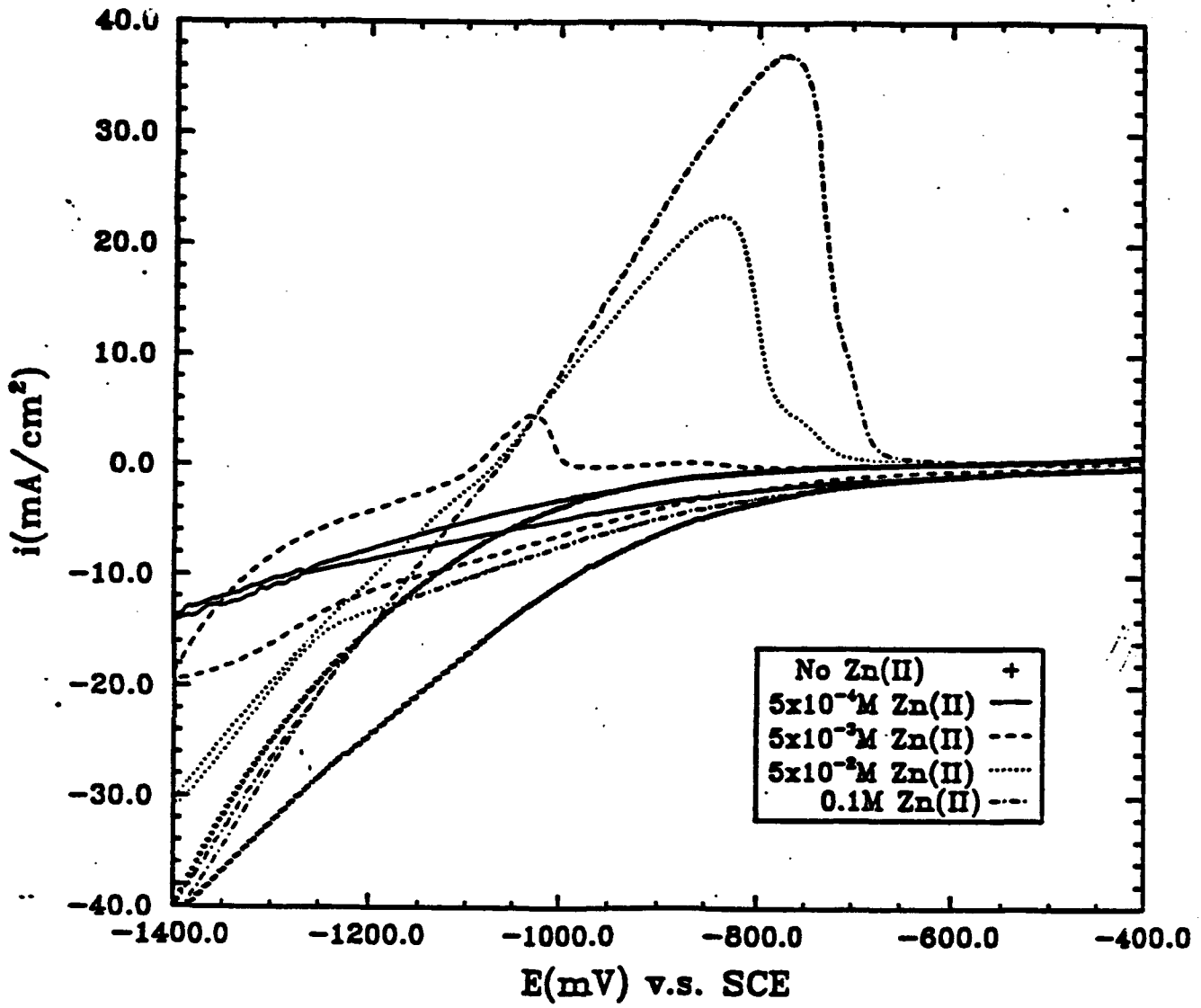
40.0
30.0
20.0
10.0
0.0
-10.0
-20.0
-30.0
-40.0
i(mA/cm²)
-1400.0
-1200.0
-1000.0
-800.0
-600.0
-400.0
E(mV) v.s. SCE
No Zn(II)
5x10⁻⁴M Zn(II)
5x10⁻³M Zn(II)
5x10⁻²M Zn(II)
0.1M Zn(II)

Figure 2

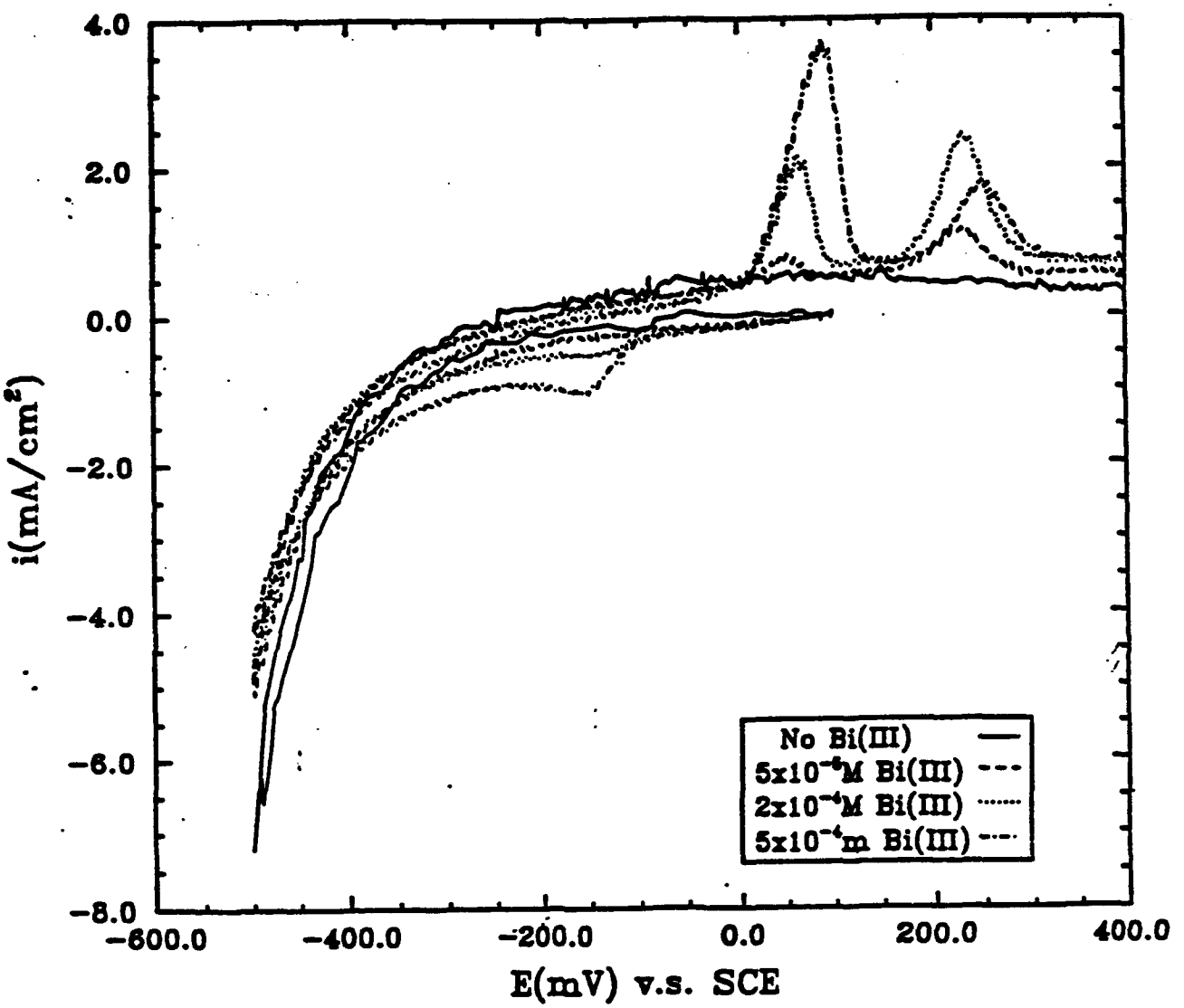
4.0
2.0
0.0
-2.0
-4.0
-6.0
-8.0
i(mA/cm²)
-600.0
-400.0
-200.0
0.0
200.0
400.0
E(mV) v.s. SCE
No Bi(III)
5x10⁻⁶M Bi(III)
2x10⁻⁴M Bi(III)
5x10⁻⁴m Bi(III)

Figure 3

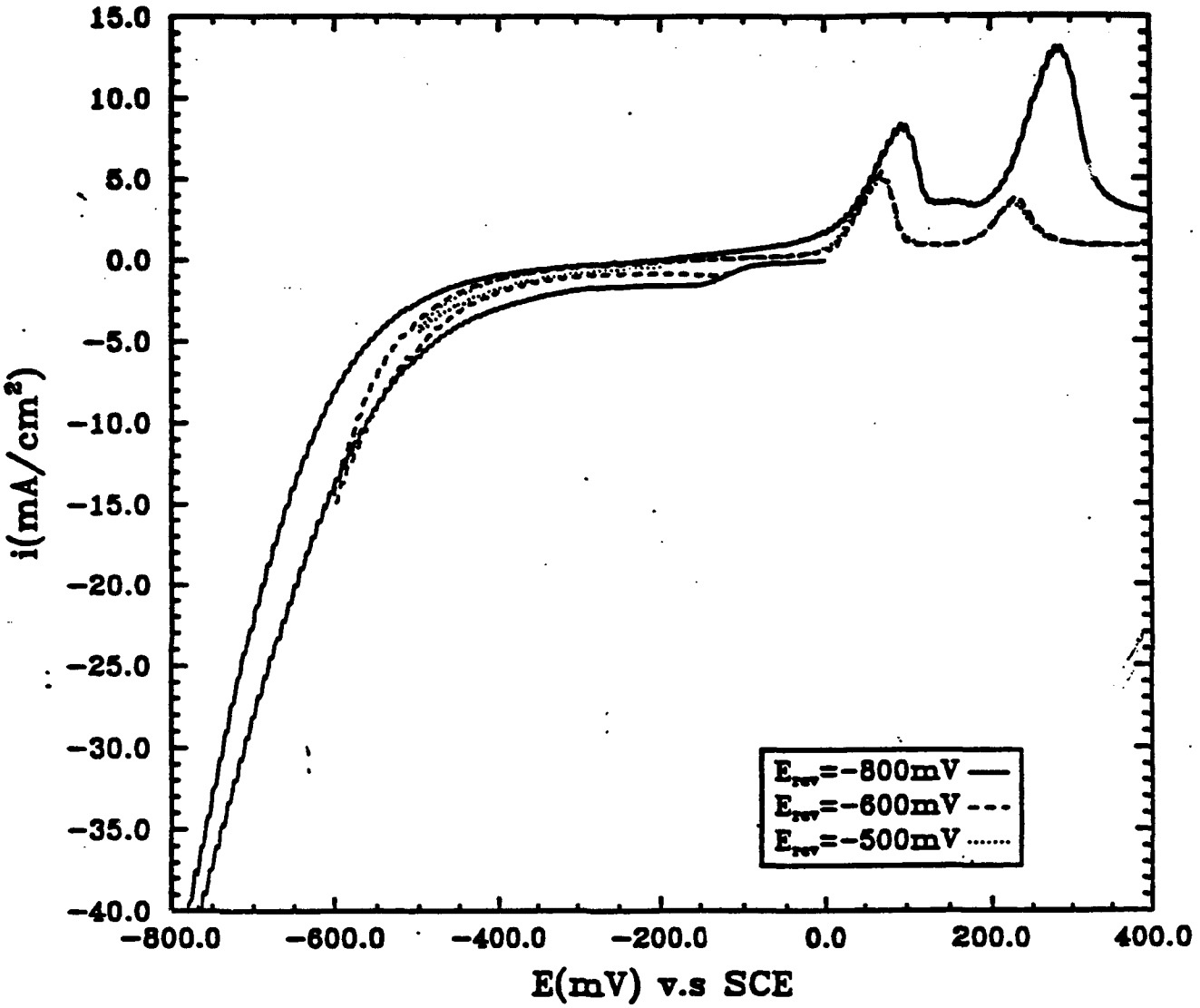
15.0
10.0
5.0
0.0
−5.0
−10.0
−15.0
−20.0
−25.0
−30.0
−35.0
−40.0
i(mA/cm²)
−800.0
−600.0
−400.0
−200.0
0.0
200.0
400.0
E(mV) v.s SCE
E_rev=-800mV
E_rev=-600mV
E_rev=-500mV

Figure 4

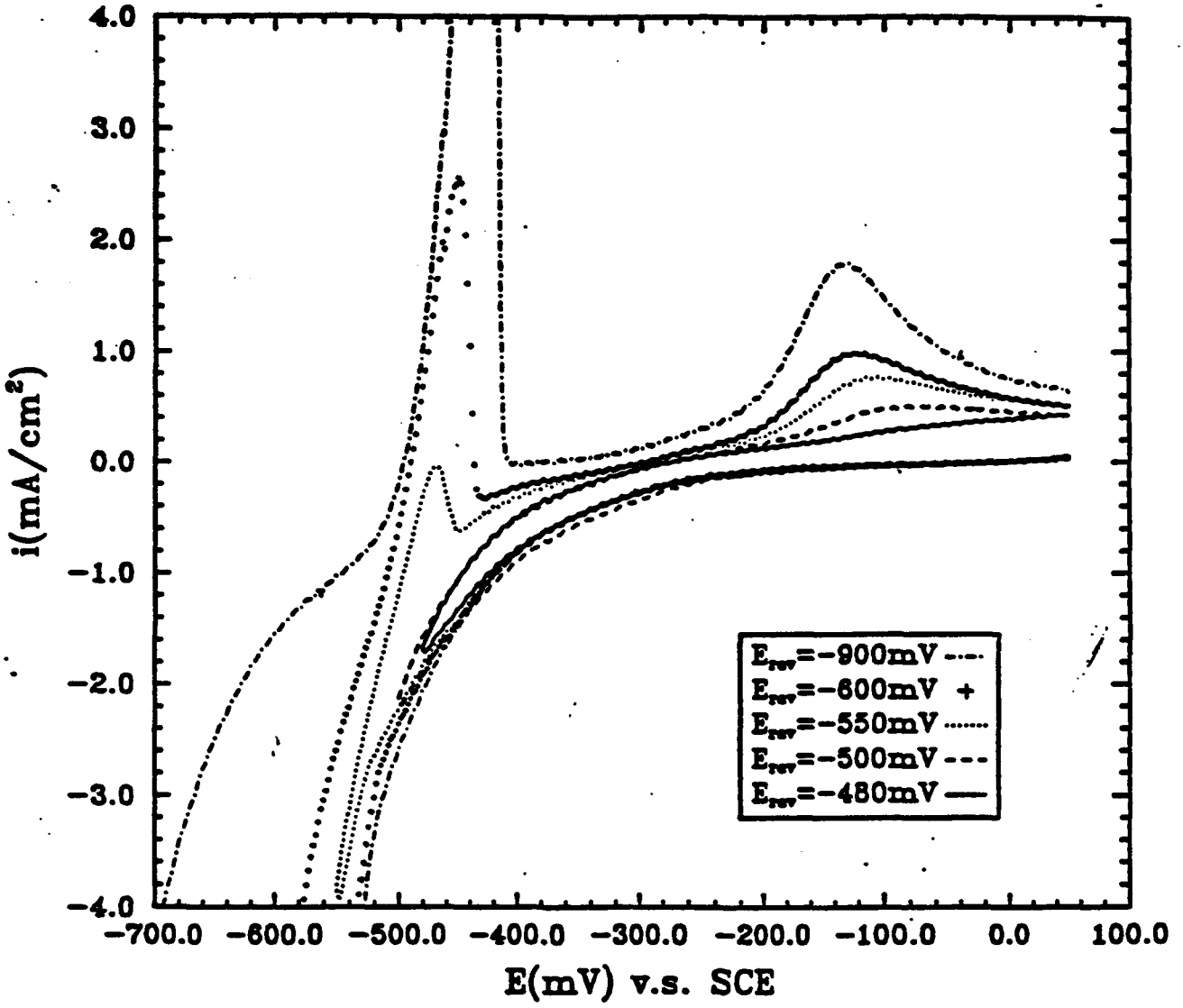
4.0
3.0
2.0
1.0
0.0
−1.0
−2.0
−3.0
−4.0
i(mA/cm²)
−700.0 −600.0 −500.0 −400.0 −300.0 −200.0 −100.0 0.0 100.0
E(mV) v.s. SCE
E_rev=−900mV
E_rev=−600mV
E_rev=−550mV
E_rev=−500mV
E_rev=−480mV

Figure 5

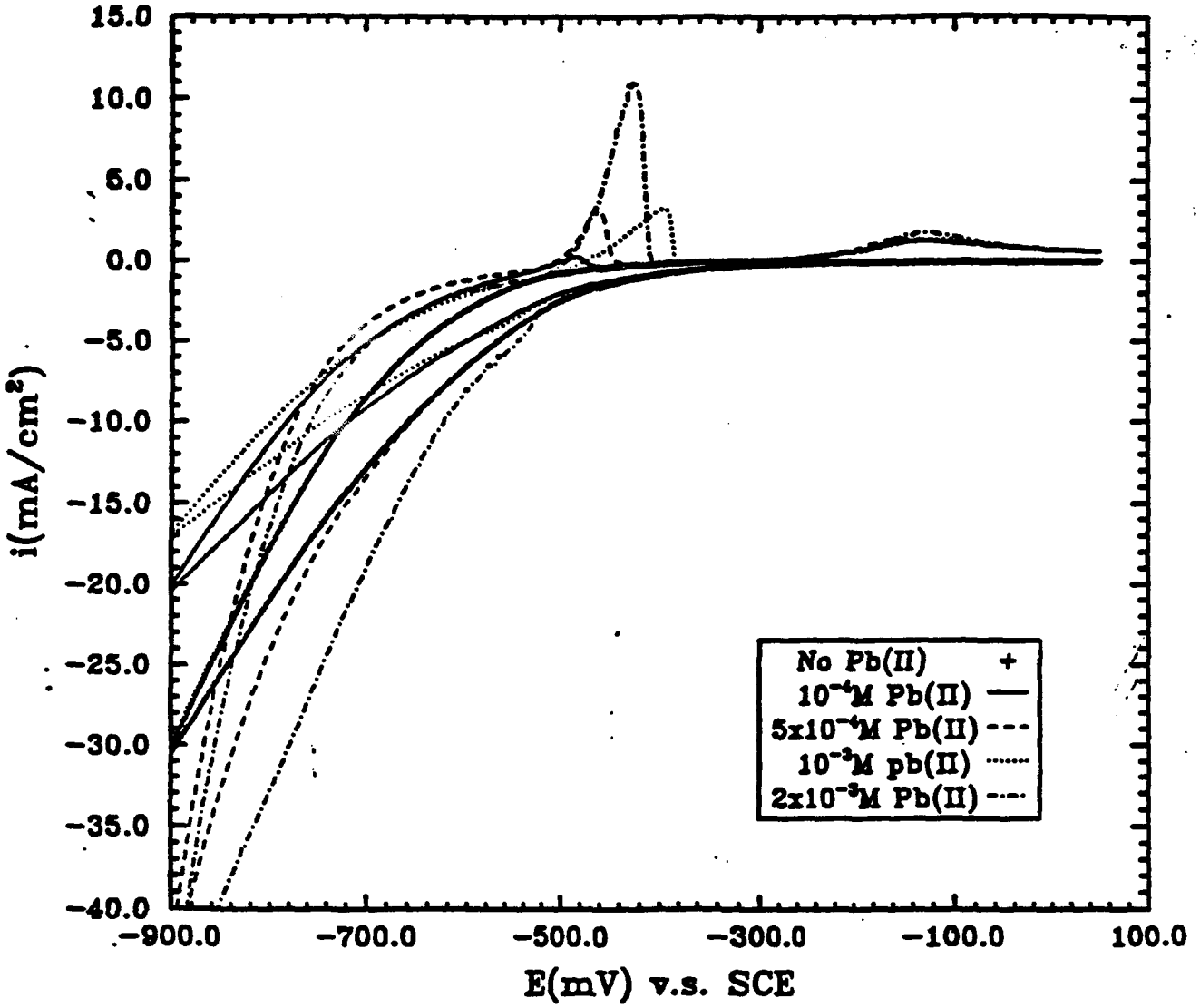
15.0
10.0
5.0
0.0
-5.0
-10.0
-15.0
-20.0
-25.0
-30.0
-35.0
-40.0
i(mA/cm²)
-900.0
-700.0
-500.0
-300.0
-100.0
100.0
E(mV) v.s. SCE
No Pb(II)
10⁻⁴M Pb(II)
5x10⁻⁴M Pb(II)
10⁻³M pb(II)
2x10⁻³M Pb(II)

Figure 6

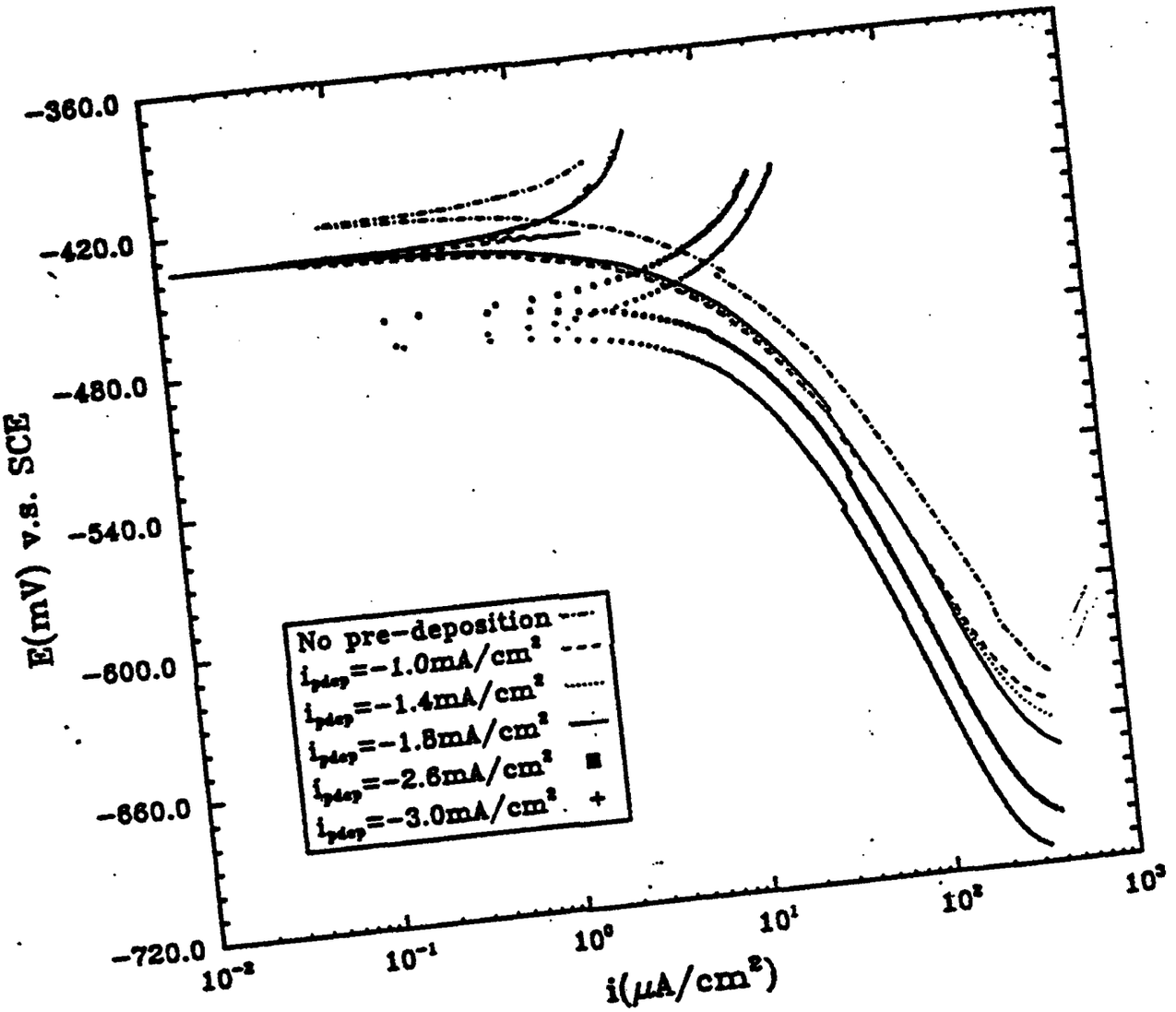
-360.0
-420.0
-480.0
-540.0
-600.0
-660.0
-720.0
E(mV) v.s. SCE
10⁻²
10⁻¹
10⁰
10¹
10²
10³
i(μA/cm²)
No pre-deposition
i_pdep=-1.0mA/cm²
i_pdep=-1.4mA/cm²
i_pdep=-1.8mA/cm²
i_pdep=-2.6mA/cm²
i_pdep=-3.0mA/cm²

Figure 7

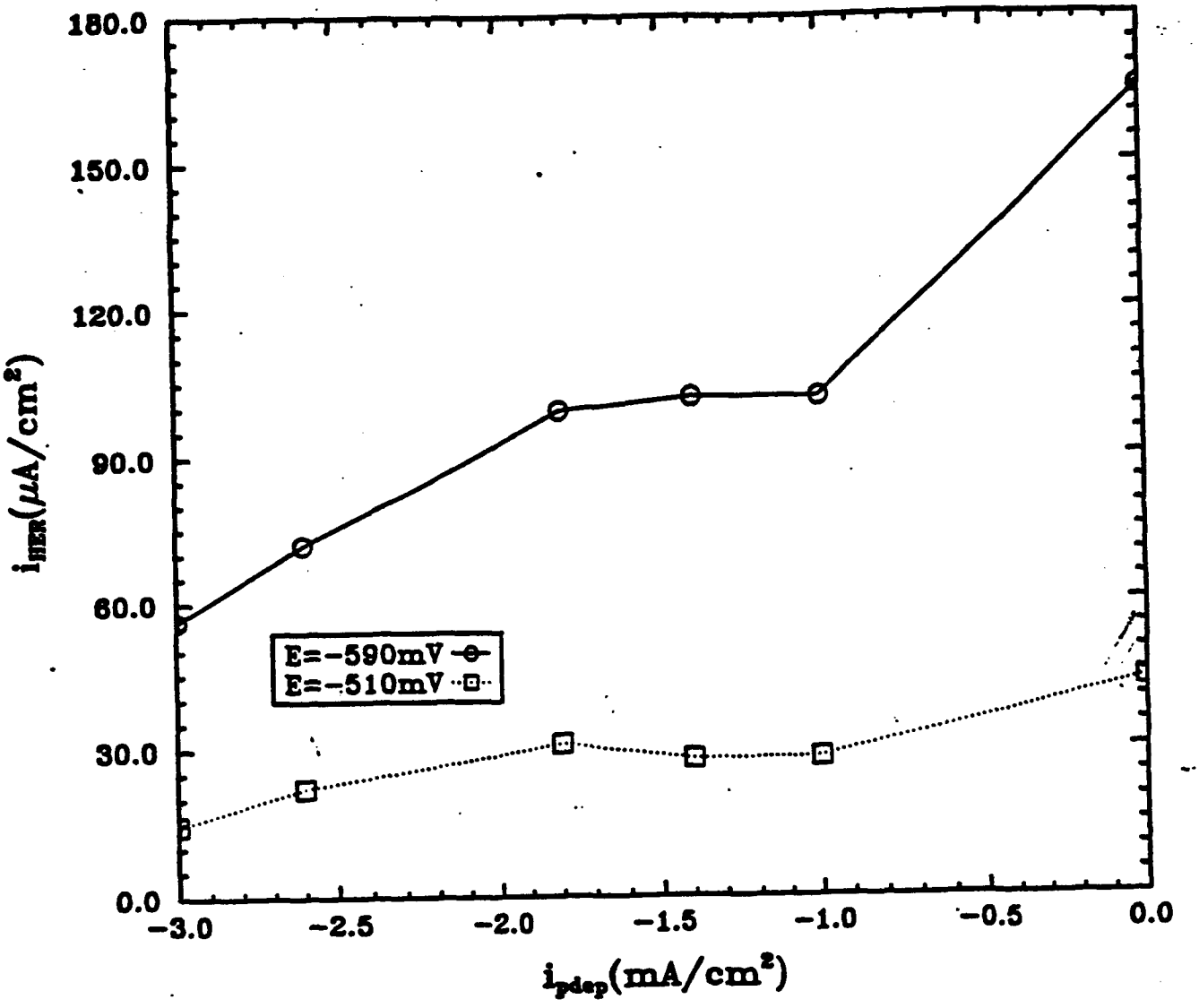
180.0
150.0
120.0
90.0
60.0
30.0
0.0
$i_{HER}(\mu A/cm^2)$
E=-590mV
E=-510mV
-3.0
-2.5
-2.0
-1.5
-1.0
-0.5
0.0
$i_{pdep}(mA/cm^2)$

Figure 8

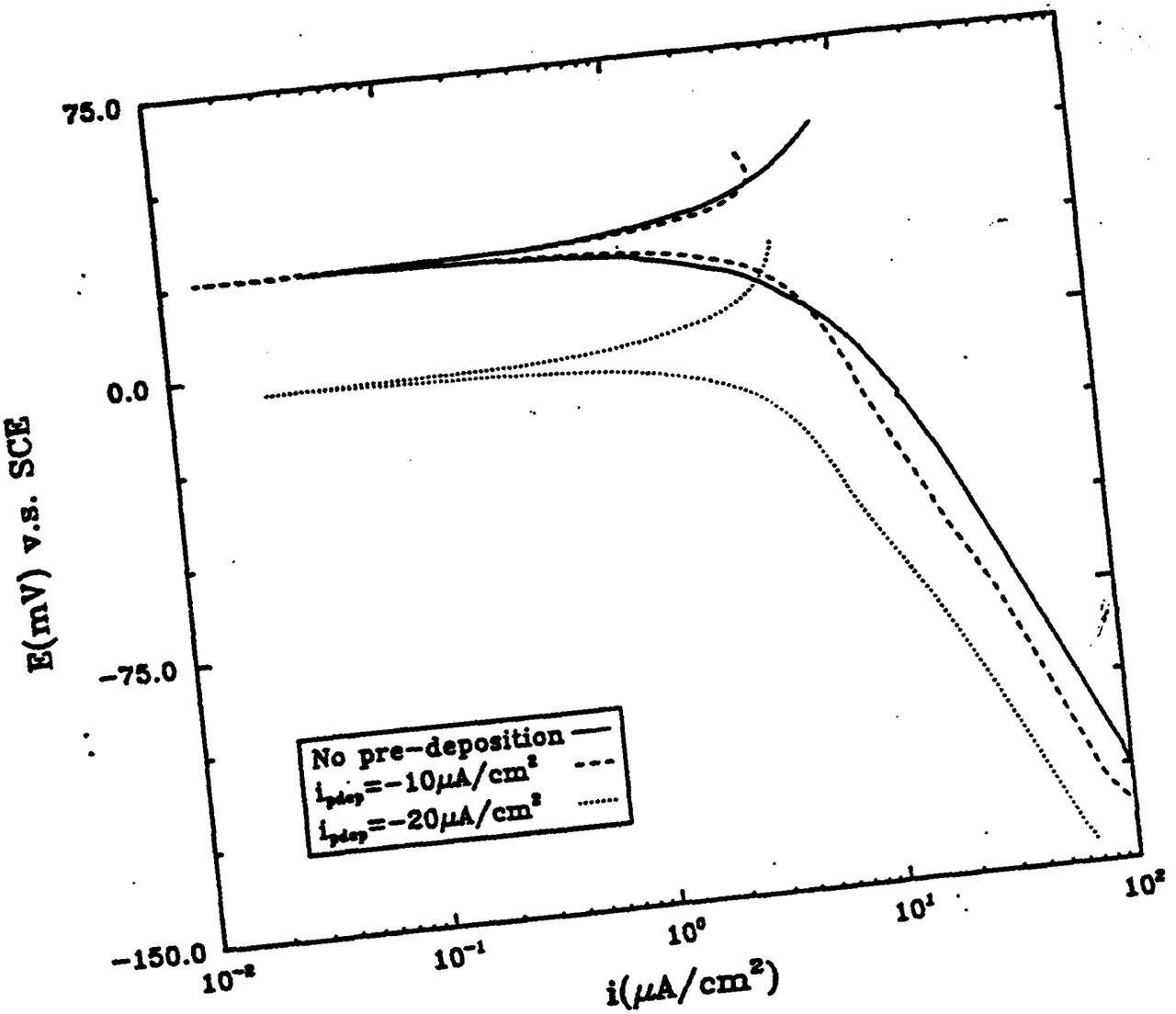
75.0
0.0
−75.0
−150.0
E(mV) v.s. SCE
10⁻²
10⁻¹
10⁰
10¹
10²
i(μA/cm²)
No pre-deposition
i_pdep=−10μA/cm²
i_pdep=−20μA/cm²

Figure 9

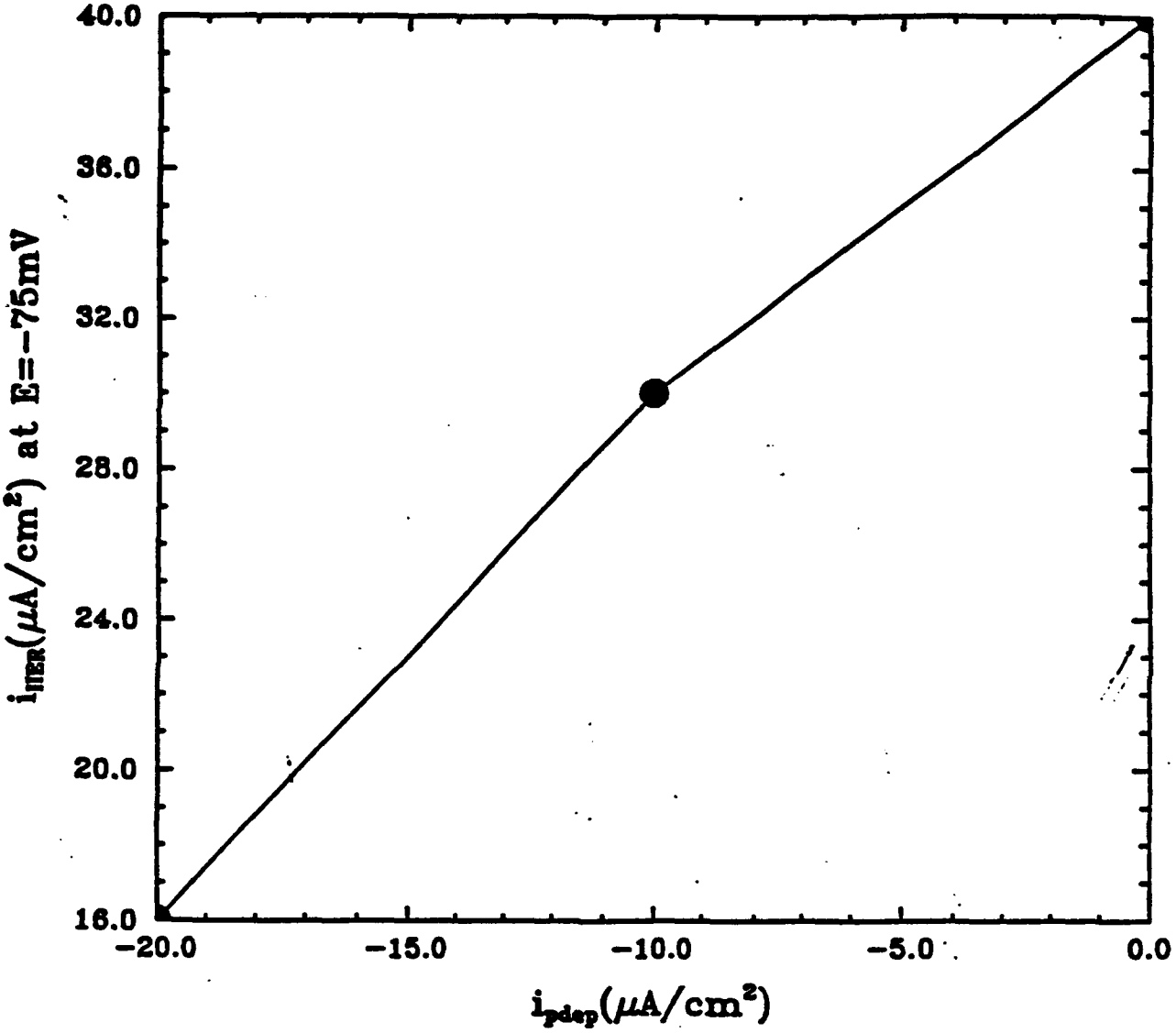
40.0
36.0
32.0
28.0
24.0
20.0
16.0
$i_{INER}(\mu A/cm^2)$ at E=−75mV
−20.0
−15.0
−10.0
−5.0
0.0
$i_{pdep}(\mu A/cm^2)$

Figure 10

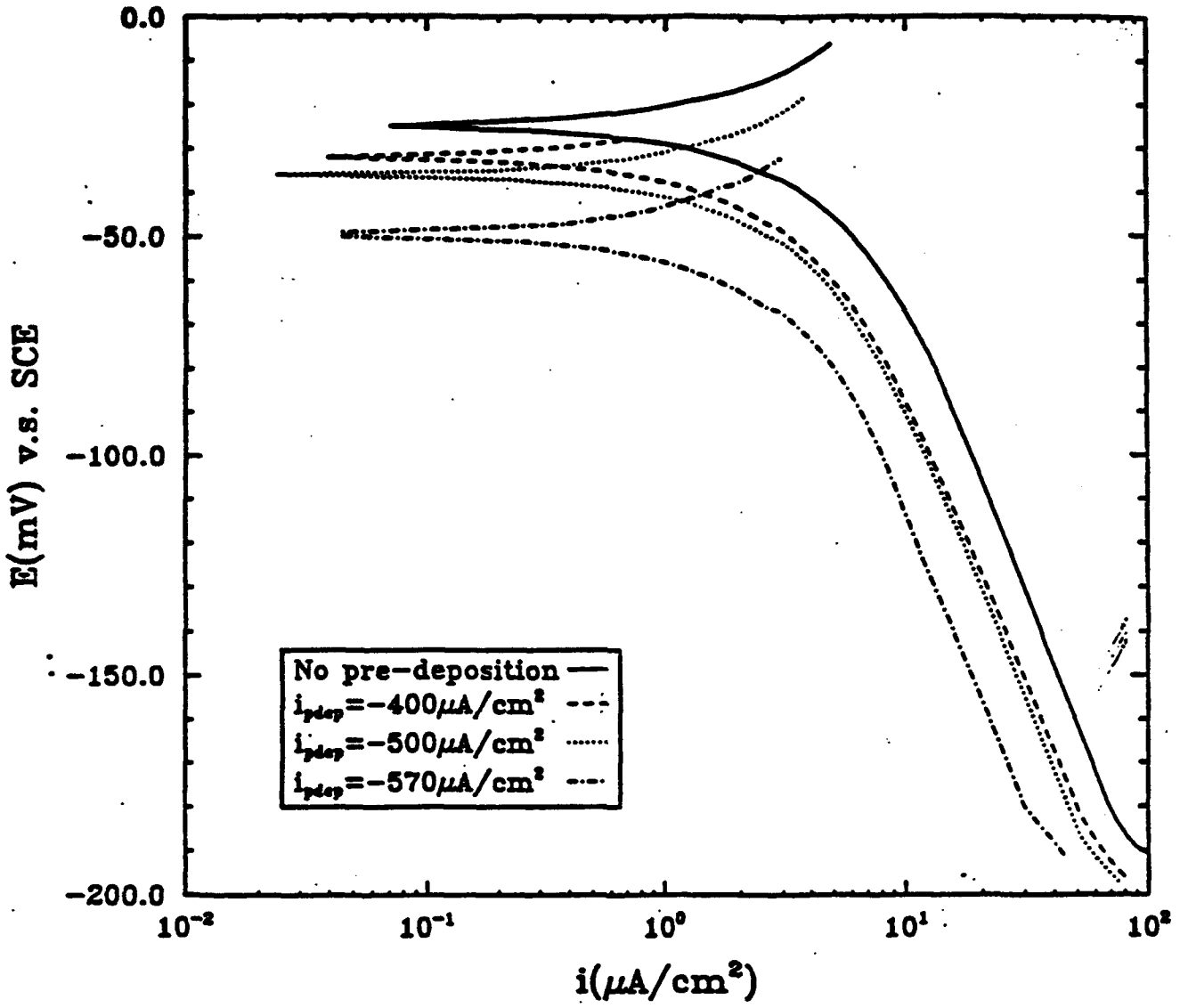
0.0
-50.0
-100.0
-150.0
-200.0
E(mV) v.s. SCE
10^{-2}
10^{-1}
10^{0}
10^{1}
10^{2}
i(μA/cm^2)
No pre-deposition
i_{pdep}=-400μA/cm^2
i_{pdep}=-500μA/cm^2
i_{pdep}=-570μA/cm^2

Figure 11

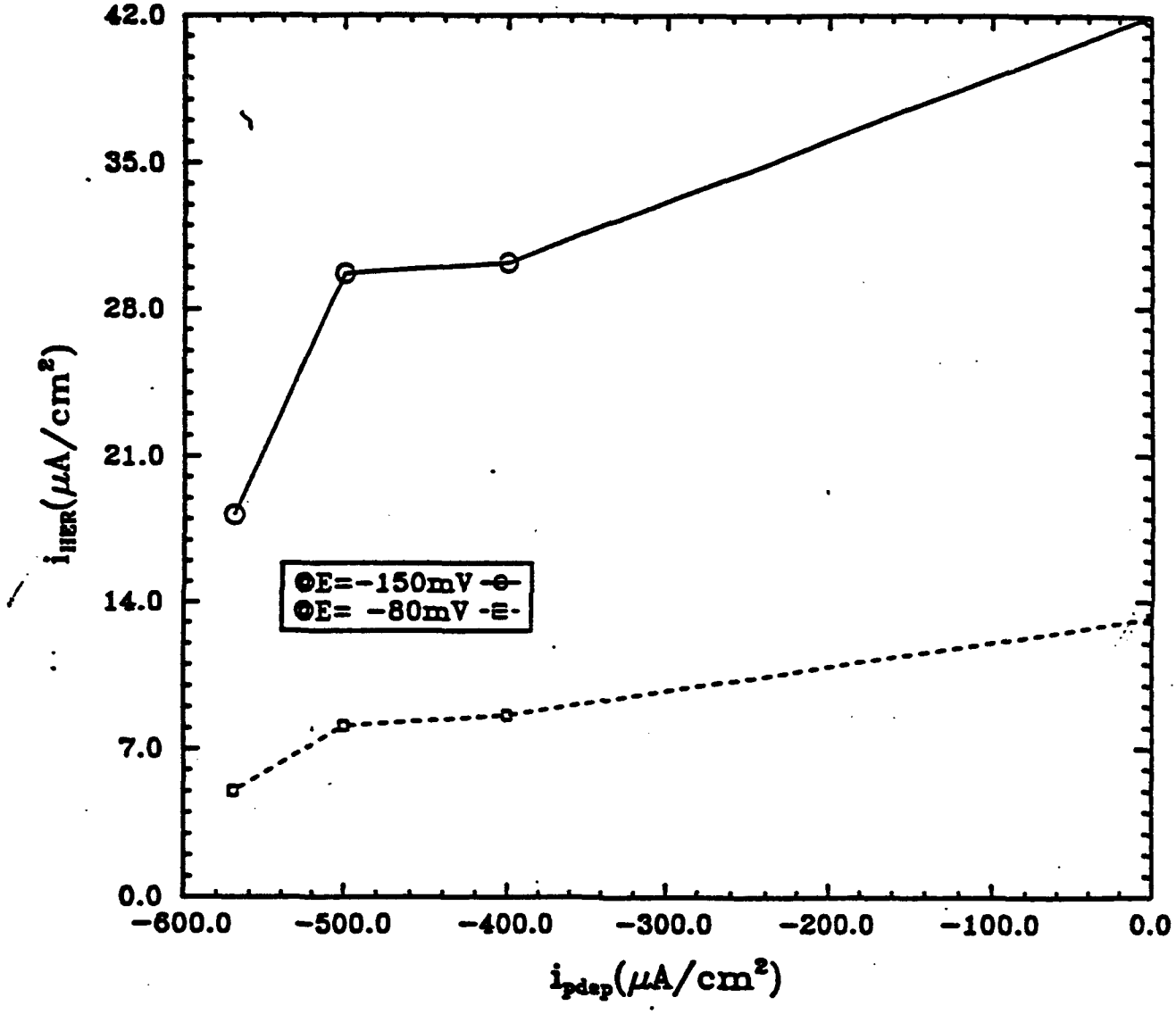
42.0
35.0
28.0
21.0
14.0
7.0
0.0
$i_{HER}(\mu A/cm^2)$
E=-150mV
E= -80mV
-600.0
-500.0
-400.0
-300.0
-200.0
-100.0
0.0
$i_{pdep}(\mu A/cm^2)$

Figure 12

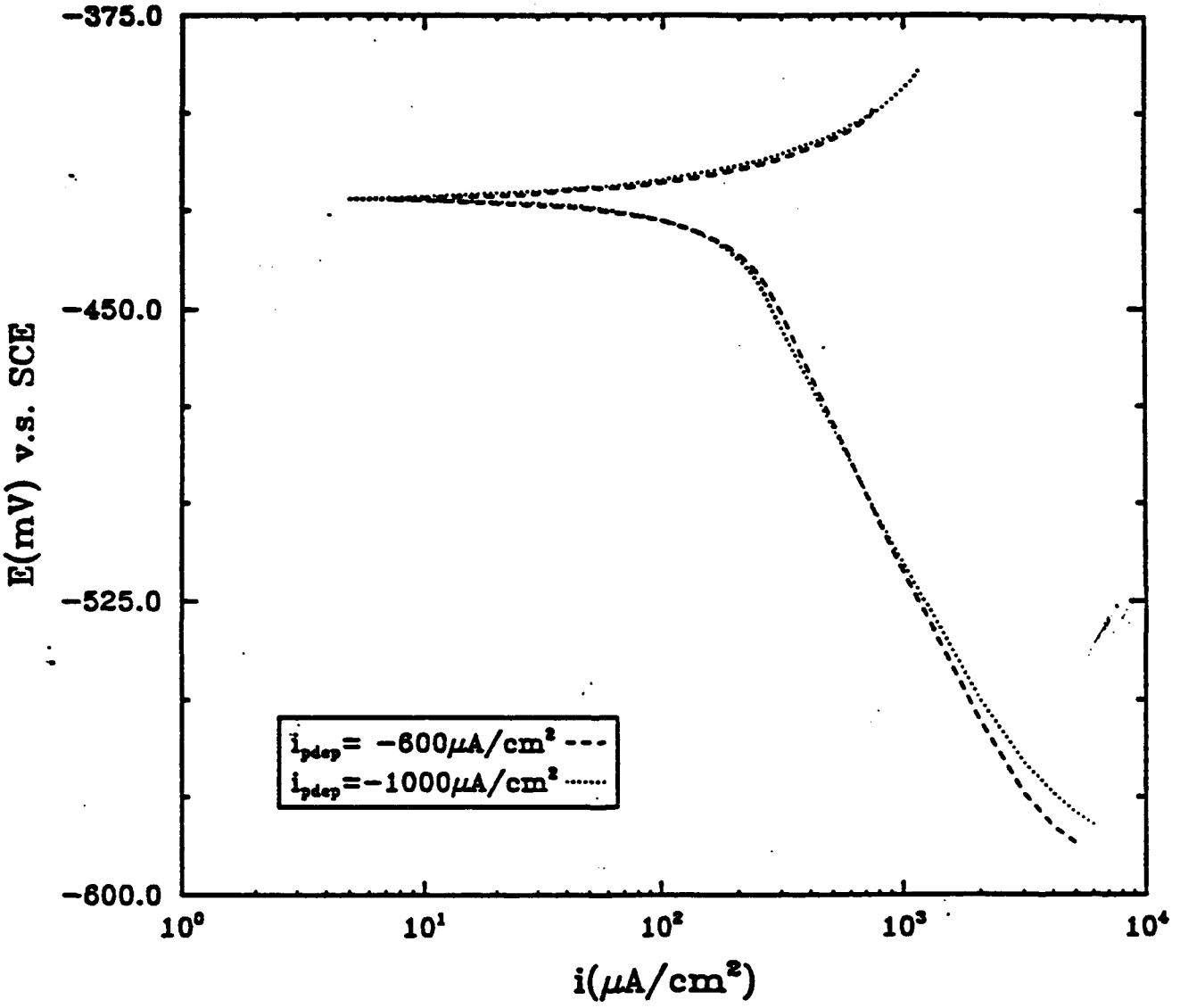
-375.0
-450.0
-525.0
-600.0
E(mV) v.s. SCE
10^0
10^1
10^2
10^3
10^4
i(μA/cm^2)
i_{pdep}= -600μA/cm^2 ---
i_{pdep}=-1000μA/cm^2 .....

Figure 13

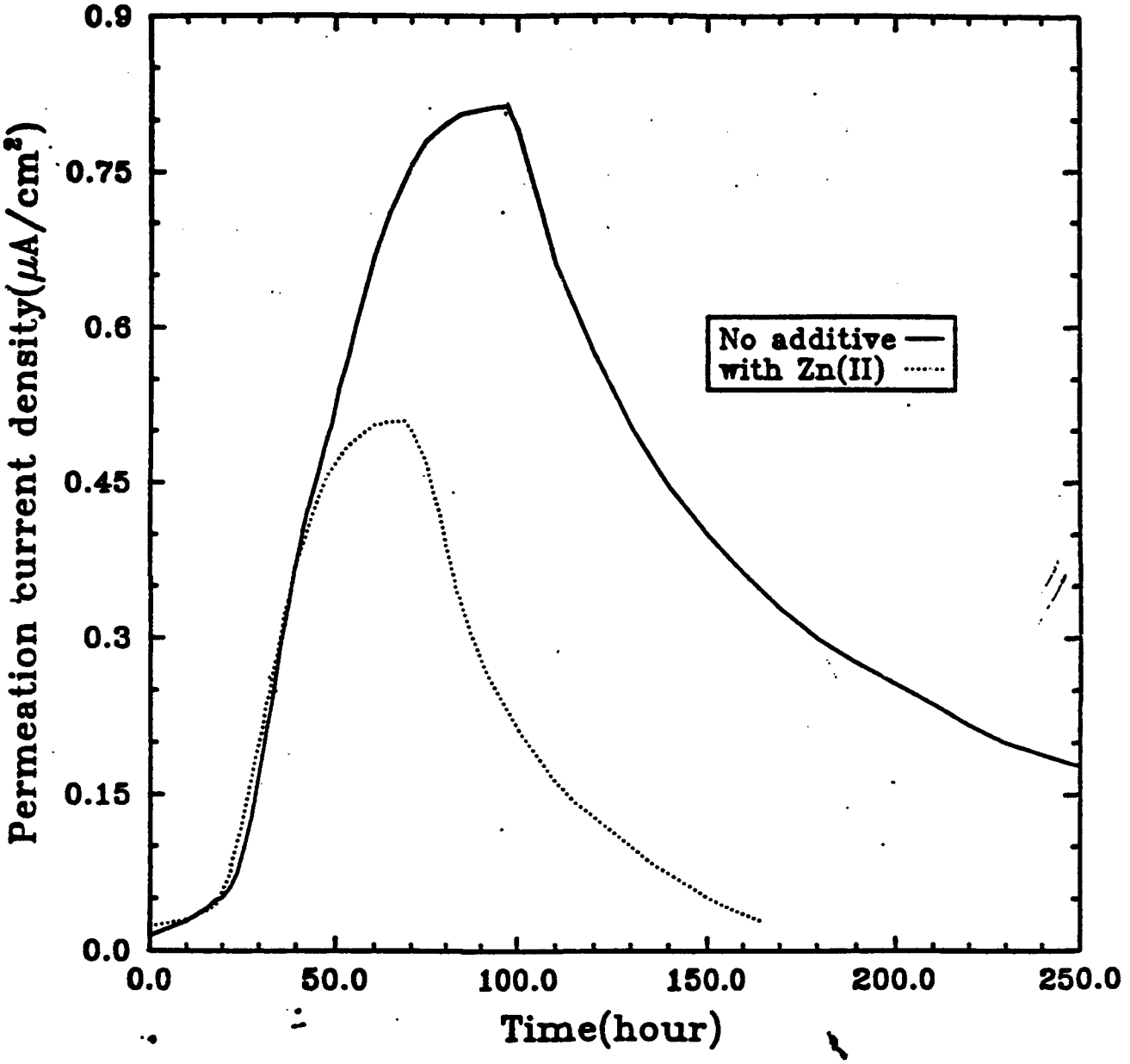
0.9
0.75
0.6
0.45
0.3
0.15
0.0
Permeation current density(μA/cm²)
0.0
50.0
100.0
150.0
200.0
250.0
Time(hour)
No additive
with Zn(II)

Figure 14

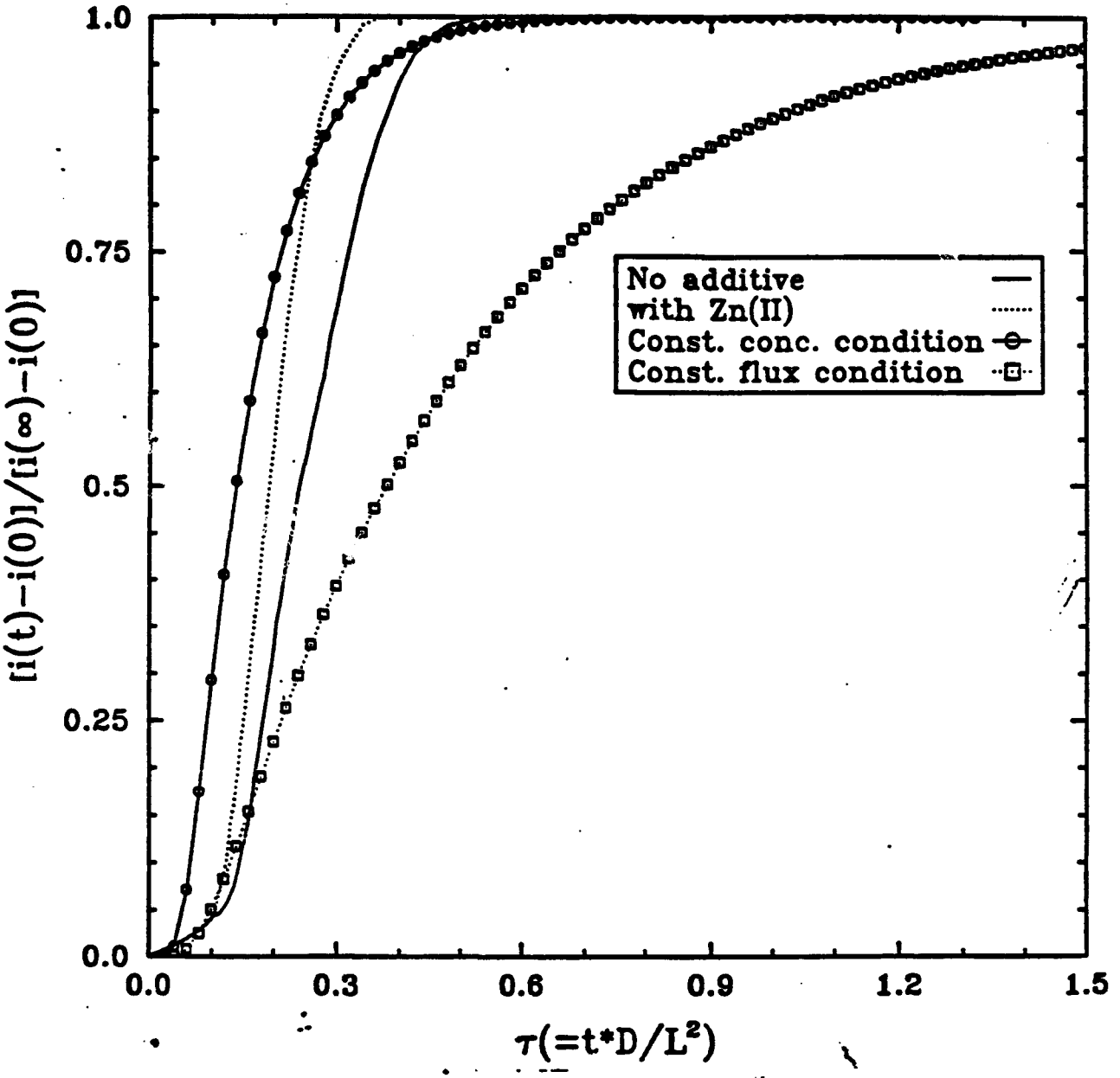
1.0
0.75
0.5
0.25
0.0
0.0
0.3
0.6
0.9
1.2
1.5
[i(t)−i(0)]/[i(∞)−i(0)]
τ(=t*D/L²)
No additive
with Zn(II)
Const. conc. condition
Const. flux condition

Figure 15

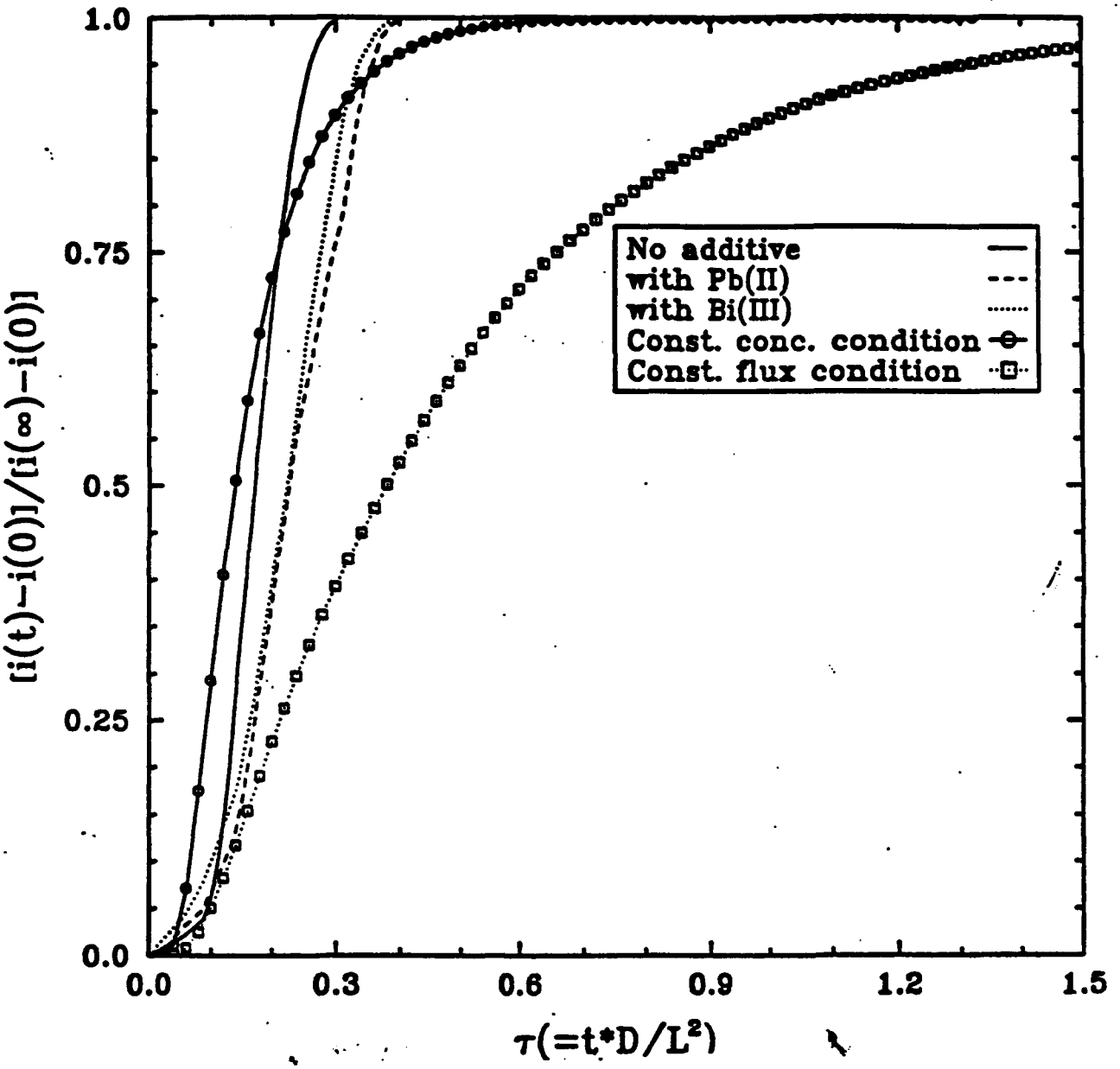
1.0
0.75
0.5
0.25
0.0
0.0
0.3
0.6
0.9
1.2
1.5
[i(t)-i(0)]/[i(∞)-i(0)]
τ(=t*D/L²)
No additive
with Pb(II)
with Bi(III)
Const. conc. condition
Const. flux condition

Figure 16

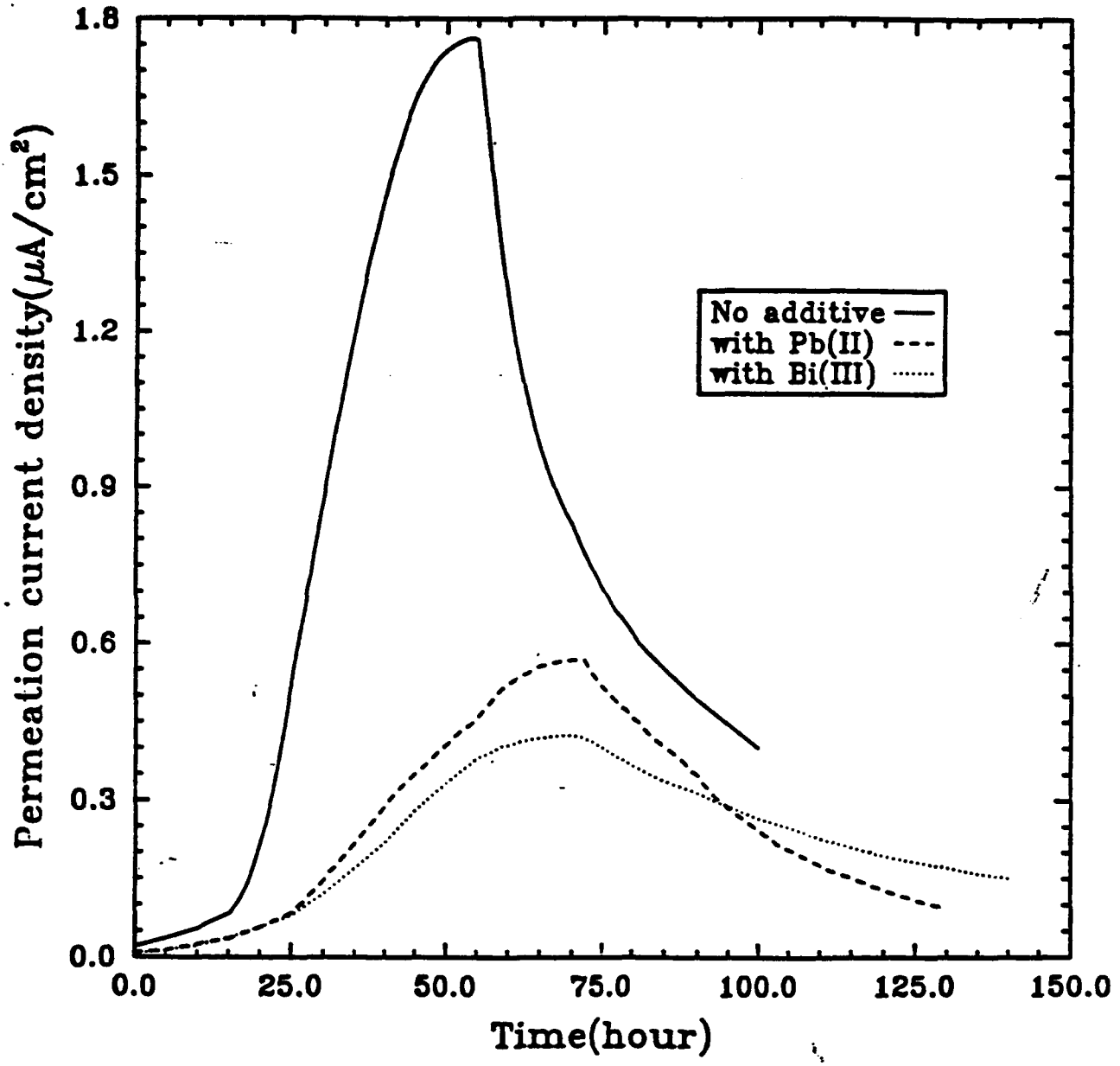
Permeation current density(μA/cm²)
1.8
1.5
1.2
0.9
0.6
0.3
0.0
0.0
25.0
50.0
75.0
100.0
125.0
150.0
Time(hour)
No additive
with Pb(II)
with Bi(III)

Figure 17